

Observation of anti-damping spin-orbit torques generated by in-plane and out-of-plane spin polarizations in MnPd₃

Mahendra DC (✉ mdc2019@stanford.edu)

Stanford University <https://orcid.org/0000-0003-1249-336X>

Ding-Fu Shao

University of Nebraska

Vincent Hou

Taiwan Semiconductor Manufacturing Company (Taiwan)

Patrick Quarterman

NIST Center for Neutron Research <https://orcid.org/0000-0001-6272-6243>

Ali Habiboglu

University of Arizona

Brooks Venuti

Colorado School of Mines

Masashi Miura

Seikei University

Brian Kirby

NIST <https://orcid.org/0000-0003-2472-3791>

Arturas Vailionis

Stanford Nano Shared Facilities, Stanford University <https://orcid.org/0000-0001-5878-1864>

Chong Bi

Institute of Microelectronics Chinese Academy of Science

Xiang Li

Stanford University

Fen Xue

Stanford University

Yen-Lin Huang

TSMC

Yong Deng

Stanford University

Shy-Jay Lin

Taiwan Semiconductor Manufacturing Company (Taiwan)

Wilman Tsai

Stanford University

Serena Eley

Colorado School of Mines <https://orcid.org/0000-0002-2928-5316>

Weigang Wang

University of Arizona

Julie Borchers

NCNR/NIST <https://orcid.org/0000-0002-3348-8212>

Evgeny Tsymbal

University of Nebraska–Lincoln <https://orcid.org/0000-0002-6728-5480>

Shan Wang

Stanford University

Article

Keywords: Magnetic Memory, Logic Devices, External Magnetic Field-free Switching, Practical Spin Channel

Posted Date: January 8th, 2021

DOI: <https://doi.org/10.21203/rs.3.rs-132828/v1>

License:  This work is licensed under a Creative Commons Attribution 4.0 International License.

[Read Full License](#)

1 **Observation of anti-damping spin-orbit torques generated** 2 **by in-plane and out-of-plane spin polarizations in MnPd₃**

3
4 Mahendra DC^{1*}, Ding-Fu Shao², Vincent D.-H. Hou³, P. Quarterman⁴, Ali Habiboglu⁵, Brooks
5 Venuti⁶, Masashi Miura^{1,7}, Brian Kirby⁴, Arturas Vailionis^{8,9}, Chong Bi¹⁰, Xiang Li^{1,10}, Fen
6 Xue¹, Yen-Lin Huang³, Yong Deng¹, Shy-Jay Lin³, Wilman Tsai¹, Serena Eley⁶, Weigang
7 Wang⁵, Julie A. Borchers⁴, Evgeny Y. Tsymbal², and Shan X. Wang^{1,10*}

8 ¹Department of Materials Science and Engineering, Stanford University, Stanford, California 94305, USA

9 ²Department of Physics and Astronomy & Nebraska Center for Materials and Nanoscience, University of Nebraska,
10 Lincoln, NE 68588-0299

11 ³Taiwan Semiconductor Manufacturing Company, Hsinchu, Taiwan

12 ⁴NIST Center for Neutron Research, National Institute of Standards and Technology, 100 Bureau Dr., Gaithersburg,
13 Maryland 20899, USA

14 ⁵Department of Physics, University of Arizona, Tucson, Arizona 85721, USA

15 ⁶Department of Physics, Colorado School of Mines, Golden, Colorado 80401

16 ⁷Graduate School of Science and Technology, Seikei University, 3-3-1 Kichijoji-kitamachi, Musashinoshi, Tokyo,
17 180-8633, Japan

18 ⁸Stanford Nano Shared Facilities, Stanford University, Stanford, CA 94305, USA

19 ⁹Department of Physics, Kaunas University of Technology, LT-51368 Kaunas, Lithuania

20 ¹⁰Department of Electrical Engineering, Stanford University, Stanford, California 94305, USA

21
22
23 **High spin-orbit torques (SOTs) generated by topological materials and heavy metals**
24 **interfaced with a ferromagnetic layer show promise for next generation magnetic memory**
25 **and logic devices. SOTs generated from the in-plane spin polarization along y-axis**
26 **originated by the spin Hall and Edelstein effects can switch magnetization collinear with**
27 **the spin polarization in the absence of external magnetic fields. However, an external**
28 **magnetic field is required to switch the magnetization along x and z-axes via SOT**
29 **generated by y-spin polarization. Here, we present that the above limitation can be**
30 **circumvented by unconventional SOT in magnetron-sputtered thin film MnPd₃. In**

31 addition to the conventional in-plane anti-damping-like torque due to the y -spin
32 polarization, out-of-plane and in-plane anti-damping-like torques originating from z -spin
33 and x -spin polarizations, respectively have been observed at room temperature. The spin
34 torque efficiency (θ_y) corresponding to the y -spin polarization from MnPd_3 thin films
35 grown on thermally oxidized silicon substrate and post annealed at 400 °C is 0.34 - 0.44
36 while the spin conductivity (σ_{zx}^y) is $\sim 5.70 - 7.30 \times 10^5 \hbar/2e \Omega^{-1}\text{m}^{-1}$. Remarkably, we have
37 demonstrated complete external magnetic field-free switching of perpendicular Co layer
38 via unconventional out-of-plane anti-damping-like torque from z -spin polarization. Based
39 on the density functional theory calculations, we determine that the observed x - and z - spin
40 polarizations with the in-plane charge current are due to the low symmetry of the (114)
41 oriented MnPd_3 thin films. Taken together, the new material reported here provides a path
42 to realize a practical spin channel in ultrafast magnetic memory and logic devices.

43

44 *Corresponding authors: mdc2019@stanford.edu and sxwang@stanford.edu

45

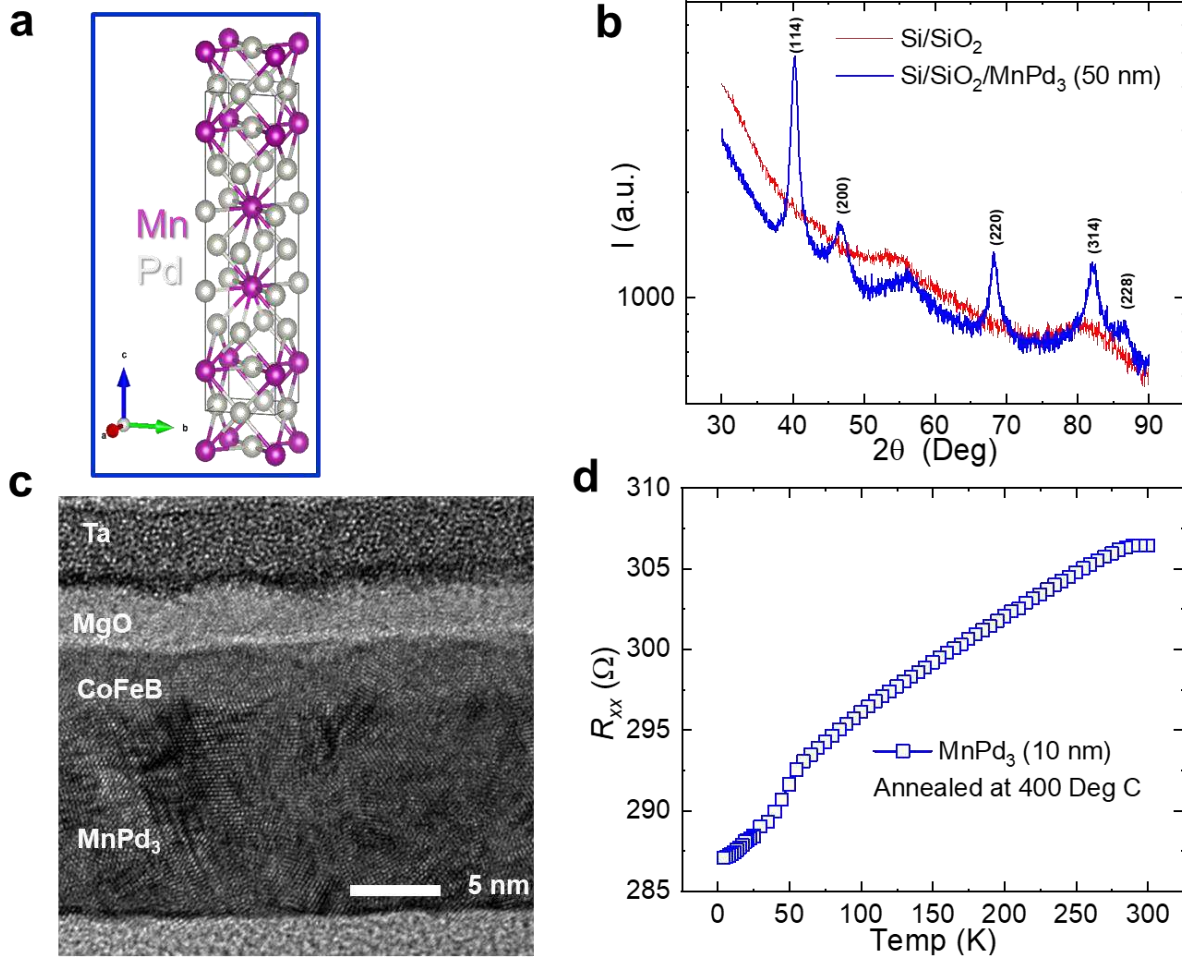
46 Efficient control of magnetization at ultra-high speed has been of prime interest to the
 47 spintronics community¹. Spin-orbit torque (SOT) has provided efficient and ultrafast control of
 48 magnetization in magnetoresistive random access memory (MRAM) and logic devices^{2,3}. SOT
 49 has been observed in magnetic semiconductor⁴ and heavy metals⁵⁻⁷, topological insulators⁸⁻¹²,
 50 antiferromagnets¹³⁻¹⁷, and semimetals¹⁸⁻²⁰ interfaced with a ferromagnetic layers. The charge
 51 current injected into the non-magnetic layer (spin channel) along the x -direction generates a spin
 52 current along z -direction with spin polarization ($\hat{\sigma}$) pointing along y -direction ($\hat{\sigma}_y$) in heavy
 53 metals due to the bulk spin Hall effect. In the case of topological insulators and Weyl semimetals
 54 non-equilibrium spin-density is accumulated at the interface due to the time reversal symmetry
 55 protected spin momentum locking²¹. SOTs exerted on the ferromagnet with in-plane magnetic
 56 anisotropy (IMA) are in-plane anti-damping-like ($\boldsymbol{\tau}_{ADL,y} \propto \hat{m} \times (\hat{\sigma}_y \times \hat{m})$) and out-of-plane
 57 field-like ($\boldsymbol{\tau}_{FL} \propto \hat{\sigma}_y \times \hat{m}$), where \hat{m} is magnetization unit vector. Spin current with $\hat{\sigma}$ along z -
 58 direction ($\hat{\sigma}_z$) has been observed in transition-metal dichalcogenides^{18,20,22} and, ferromagnets
 59 interfaced with light metals²³ with the charge current flow along x -direction. SOT due to $\hat{\sigma}_z$
 60 exerts torque along the out-of-plane direction ($\boldsymbol{\tau}_{ADL,z} \propto \hat{m} \times (\hat{\sigma}_z \times \hat{m})$), which will enable
 61 external field free and low power switching of the out-of-plane magnetization²⁴. Recently, $\hat{\sigma}$
 62 along the x -direction ($\hat{\sigma}_x$) has been reported in the uncompensated antiferromagnet Mn₃GaN in
 63 addition to $\hat{\sigma}_y$ and $\hat{\sigma}_z$ due to the low magnetic symmetry¹⁷. SOT due to $\hat{\sigma}_x$ exerts torque along in-
 64 plane direction ($\boldsymbol{\tau}_{ADL,x} \propto \hat{m} \times (\hat{\sigma}_x \times \hat{m})$), which will deterministically switch the magnetization
 65 along the x -direction in the absence of external magnetic field. The figure of merit of charge to
 66 spin conversion is known as the spin torque efficiency $\theta_k \propto \frac{\sigma_{ij}^k}{\sigma_{xx}}$, where σ_{ij}^k (i, j , and k refers to
 67 the spin current flow, charge current flow, and spin polarization directions, respectively) and σ_{xx}

68 are spin and charge conductivities, respectively. θ_k needs to be high for efficient control of the
69 magnetization. Furthermore, to avoid current shunting through a conducting ferromagnetic layer
70 high σ_{ij}^k is also required²⁵. Another important requirement for the integration of a spin channel
71 into semiconductor IC technology is the tolerance of SOT materials to thermal annealing at 400
72 °C. However, there has not been a practical spin channel which can handle post annealing at that
73 temperature, and also possesses high $\tau_{ADL,y}$ along with $\tau_{ADL,x}$ and $\tau_{ADL,z}$, enabling deterministic
74 switching of in-plane magnetization along y , in-plane magnetization along x , and out-of-plane
75 magnetization, respectively, without the need of applying an external magnetic field.

76 To achieve high density magnetic memory and logic devices, perpendicular magnetic
77 anisotropy (PMA) is desired²⁶. PMA switching via SOT from heavy metals⁵⁻⁷ and topological
78 insulators^{11,12,27,28} has been reported at the room temperature in the presence of an external
79 magnetic field. Partial PMA switching has been observed on PtMn/[Co/Ni]_x¹³, IrMn/CoFeB¹⁴,
80 and PtMn/CoFeB/Gd/CoFeB¹⁶ stack structures, in the absence of external magnetic field, but
81 with the help of exchange bias. Stray fields from an in-plane magnetic layer present above or
82 below the spin channel can facilitate external magnetic field-free PMA switching, but current
83 shunting and magnetic interference between different magnetic layers pose severe design
84 constraints in this approach^{29,30}. Combination of SOT and spin transfer torque (STT) can also
85 switch PMA in the absence of external magnetic field, but STT could lead to reduced endurance
86 of magnetic tunnel barrier and slower magnetization switching³¹. Fast switching of the
87 magnetization with lower critical current densities (J_{sw}) can be achieved when the charge
88 current flow and magnetization are collinear, however, this geometry still requires an external
89 magnetic field to achieve magnetization switching⁷. Here, we present SOT from sputtered MnPd₃
90 thin films post annealed at 400 °C that can generate a spin current with $\hat{\sigma}$ along all three axes

91 due to the charge current flow along x -direction, which represents a major advance over the
 92 literature and overcomes significant limitations of the existing SOT materials.

93



94

95

96 **Fig. 1. Characterization of MnPd₃ thin film:** **a**, Schematic diagram of D023 MnPd₃ unit cell.

97 **b**, XRD of Si/SiO₂/MnPd₃ (50 nm) film, post-annealed at 400 °C for 30 min. **c**, Cross-section

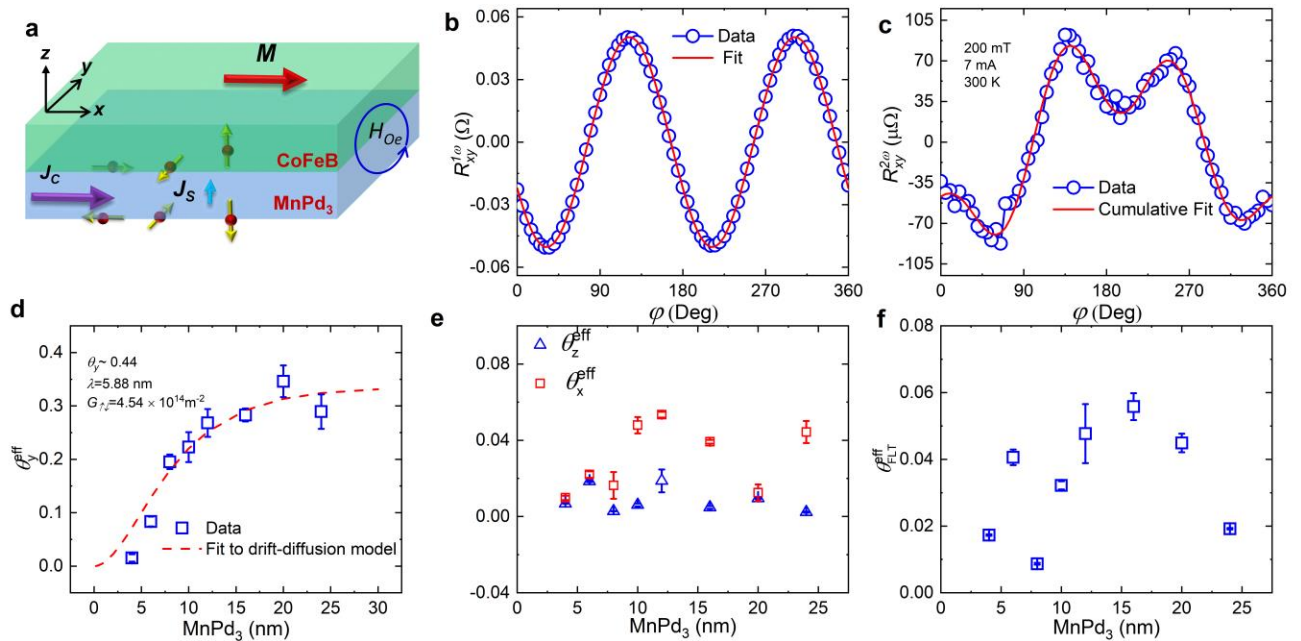
98 TEM image of Si/SiO₂/MnPd₃ (10 nm)/CoFeB (5 nm)/MgO (2 nm)/Ta (2 nm) sample. **d**, Four

99 terminal resistance as a function of temperature of Si/SiO₂/MnPd₃ (10 nm) sample.

100 The MnPd₃ thin films were magnetron sputtered at room temperature on 300 nm thick
101 thermally oxidized silicon substrates. The thin films with the stack structure Si/SiO₂/MnPd₃ (*t*
102 nm)/CoFeB (5 nm)/MgO (2 nm)/Ta (2 nm) with IMA were prepared for the SOT
103 characterization with *t* = 4, 6, 8, 10, 12, 16, 20, and 24 nm, respectively. Unless otherwise stated,
104 these films will be labeled MP4 - MP24, in which the number denotes the MnPd₃ thickness. All
105 samples were post annealed at 400 °C for 30 minutes. Using Rutherford backscattering, the
106 atomic composition of Mn and Pd in MnPd₃ film is 28% and 72% (data not shown), respectively.

107 Fig. 1a shows the unit cell of MnPd₃. We performed grazing incidence $\theta - 2\theta$ X-ray
108 diffraction (XRD) measurements on a Si/SiO₂/MnPd₃ (50 nm) sample, as shown in Fig. 1b. For
109 the grazing incidence XRD measurement Φ and Ω were fixed at 20° and 3.5°, respectively. From
110 the intensity of the peaks and pole figures (Supplementary 1 and Fig. S1), its notable that MnPd₃
111 film has a strong (114) texture. The lattice parameters are estimated to be $a = 3.89 \text{ \AA}$, $b = 3.88 \text{ \AA}$,
112 and $c = 15.42 \text{ \AA}$ indexed by using ref. (32). The cross-section transmission electron microscopy
113 (TEM) bright image of the MP10 sample is presented in Fig. 1c. The high angle annular dark
114 field (HAADF) image (data not shown) and the bright image both show that the MnPd₃ layer
115 grown on thermally oxidized silicon is polycrystalline. The CoFeB and MgO layers are also
116 polycrystalline. The electric and magnetotransport measurements were performed on
117 Si/SiO₂/MnPd₃ (10 nm)/MgO (2 nm)/Ta (2 nm) heterostructure, it will be labelled as MnPd (10
118 nm) sample (Supplementary 2 and Fig. S2). The resistivity shows metallic behavior coinciding
119 with the possible transition from a paramagnetic to an antiferromagnetic state below 50 K, as
120 shown in Fig. 1d. The ordinary Hall resistance as a function of the external magnetic field is non-
121 linear at small fields. From the high-field linear region, we estimate a carrier concentration of 4.4
122 $\times 10^{22}/\text{cm}^3$. At room temperature the values of anisotropic magnetoresistance (AMR) and planar

123 Hall resistance (PHR) are estimated to be 0.012% and 20 mΩ in MnPd (10 nm) sample,
 124 respectively. The Néel temperature of MnPd (10 nm) sample is approximately 37 K inferred
 125 from using temperature-dependent magnetometry (Supplementary 3 and Fig. S3). Polarized
 126 neutron reflectometry (PNR) measurements show weak ferromagnetism, persisting upto room
 127 temperature, in MnPd₃ films possibly originating from uncompensated Mn moments, Mn
 128 clusters, or local ferromagnetic Mn-based compound formation. At room temperature the
 129 ferromagnetic component of the magnetization in MnPd₃ is determined to be 9 ± 1.9 kA/m using
 130 polarized neutron reflection (PNR) whereas at 6 K it is $\sim 43 \pm 3.4$ kA/m (Supplementary 4 and
 131 Fig. S4).



132

133

134 **Fig. 2. SOT characterization using Second Harmonic Hall (SHH) technique on**
 135 **Si/SiO₂/MnPd₃ (x nm)/CoFeB (5 nm)/MgO (2 nm)/Ta (2 nm):** a, Schematic diagram showing
 136 in-plane charge current generated spin current with spin polarizations along three axes. The red

137 spheres represent electrons and yellow arrows represent spin magnetic moment, respectively. **b**,
 138 and **c**, $R_{xy}^{1\omega}$ and $R_{xy}^{2\omega}$, respectively, as a function of in-plane magnetic field rotation at a fixed
 139 amplitude of 200 mT in MP12 sample. **d**, **e**, and **f**, Effective spin torque efficiency due to the in-
 140 plane anti-damping-like, in-plane and out-of-plane anti-damping-like and field-like torques,
 141 respectively, as a function of MnPd₃ film thickness. The Hall bar device used for this
 142 measurement was 10 μm wide and 130 μm long, respectively.

143 We performed SOT measurements using SHH technique on MP4-MP24 samples, control
 144 MP (10 nm) and Si/SiO₂/ CoFeB (5 nm)/MgO (2 nm)/Ta (2 nm) samples, and a reference
 145 Si/SiO₂/Pt (10 nm)/CoFeB (5 nm)/MgO (2 nm)/Ta (2 nm) (labelled as Pt10 sample) sample³³.
 146 The MP4-MP24 samples and reference sample were patterned into Hall bars with length 130 and
 147 width 10 μm , respectively. The details of the SHH are presented in Supplementary 5 and Fig. S5.
 148 The a.c. current injected into the Hall bar induces effective spin-orbit fields, which oscillate the
 149 magnetization around its equilibrium position, and as a result, a SHH voltage is induced. In the
 150 SHH measurement, the sample is rotated in the x - y plane under constant static magnetic field to
 151 keep the magnetization in a single domain state. The spin current with the spin magnetic moment
 152 pointing along the negative y -axis and positive x - and z -axes get accumulated between MnPd₃ and
 153 CoFeB layers as shown in Fig. 2a. Thus, accumulated spin currents exert $\boldsymbol{\tau}_{ADL,x}$, $\boldsymbol{\tau}_{ADL,y}$ and
 154 $\boldsymbol{\tau}_{ADL,z}$, $\boldsymbol{\tau}_{FL}$ on the CoFeB layer along the in-plane and out-of-plane directions, respectively. In
 155 addition, the Oersted field (H_{oe}) generated due to the a.c. current flow in the MnPd₃ layer exerts
 156 an Oersted torque ($\boldsymbol{\tau}_{oe}$) on the CoFeB layer. Fig. 2b shows $R_{xy}^{1\omega}$ as a function of the in-plane
 157 magnetic field angle (φ). $R_{xy}^{1\omega}$ fits perfectly to the $\sin 2\varphi$, indicating that the out-of-plane field
 158 projection due to the imperfect sample mounting is absent. $R_{xy}^{2\omega}$ as a function of magnetic field
 159 angle is presented in Fig. 3c. Since the torques have different dependencies with φ , we can

160 extract $R_{xy}^{2\omega}$ due to different types of torques using SHH. In MP10 sample, the extracted spin-
 161 orbit fields associated with the $\tau_{ADL,x}$, $\tau_{ADL,y}$, $\tau_{ADL,z}$, and τ_{FL} are (0.02 ± 0.002) , $(0.132 \pm$
 162 $0.002)$, (0.0036 ± 0.0003) , and (0.019 ± 0.00) mT per 10^6 A/cm², respectively. These values of
 163 the $\tau_{ADL,y}$ and τ_{FL} are comparable or better than the previous reports on heavy
 164 metals/ferromagnet³³, TIs/ferromagnet^{11,12}, and Weyl semimetal/ferromagnets¹⁹. In Fig. 2d
 165 θ_y^{eff} as a function of MnPd₃ film thickness is presented, which shows heavy metal like behavior.
 166 The simple drift-diffusion model (Eqn. 1) can be utilized to extract bulk spin-torque efficiency
 167 figure of merit ($\theta_y(t \approx \infty)$) and spin-diffusion length (λ),

$$168 \quad \theta_y^{eff} = \theta_y(t \approx \infty) \left(1 - \operatorname{sech}\left(\frac{t}{\lambda}\right)\right) \quad (1)$$

169 where t is MnPd₃ film thickness. This drift-diffusion model considers that the spin current
 170 generated by the bulk of thin films is completely absorbed by the ferromagnetic layer without
 171 any dissipation at the interface and back-flow of the spin current. $\theta_y(t \approx \infty)$ and λ obtained by
 172 ordinary drift-diffusion model are 0.34 and 6.30 nm, respectively. Now by considering spin-back
 173 flow the drift-diffusion model can be modified into³⁴⁻³⁶:

$$174 \quad \theta_y^{eff} = \theta_y(t \approx \infty) \left(1 - \operatorname{sech}\left(\frac{t}{\lambda}\right)\right) \left[\frac{1 + \tanh\left(\frac{t}{2\lambda}\right)}{2\rho\lambda G_{\uparrow\downarrow}}\right]^{-1} \quad (2)$$

175 where ρ is bulk resistivity, $G_{\uparrow\downarrow}$ is spin-mixing conductivity, respectively. The red line in Fig. 2d
 176 is a fit to Eqn. (2) with $\theta_y(t \approx \infty)$ and λ as independent fitting parameters. $G_{\uparrow\downarrow}$ values of MP4
 177 and MP24 samples are estimated to be 4.54×10^{14} m⁻² and 3.70×10^{15} m⁻², respectively. The
 178 extracted values of $\theta_y(t \approx \infty)$ and λ are 0.44 and 5.88 nm, respectively for $G_{\uparrow\downarrow}$ value of $4.54 \times$
 179 10^{14} m⁻². ρ value used for the fitting was 60 $\mu\Omega\text{cm}$ obtained by measuring four terminal

180 resistance of Sub/MnPd₃ (20 nm)/MgO (2 nm)/Ta (2 nm) sample. The extracted values of
181 $\theta_y(t \approx \infty)$ and λ are 0.36 and 6.30 nm, respectively for $G_{\uparrow\downarrow}$ value of $3.70 \times 10^{15} \text{ m}^{-2}$. The values
182 of the σ_{zx}^y corresponding to θ_y (0.34 - 0.44) are estimated to be $(5.67 - 7.33) \times 10^5 \hbar/2e \Omega^{-1}\text{m}^{-1}$.
183 These values of σ_{zx}^y are among the largest for the reported values of the antiferromagnets^{15,37},
184 heavy metals^{6,38,39}, topological insulators^{8,11}, and Weyl semimetals¹⁹. $R_{xy}^{2\omega}$ in the control samples
185 does not show any field or φ dependence indicating that the SOTs in the MP samples originates
186 from the MnPd₃ layer (Supplementary 5 and Figs. S5 and S6). The values for the spin-orbit fields
187 associated with $\tau_{ADL,y}$ and τ_{FL} of the reference Pt10 sample are estimated to be (0.040 ± 0.003)
188 and (0.012 ± 0.001) mT per 10^6 A/cm^2 , respectively (Supplementary 7 and Fig. S7). The
189 estimated value of θ_y^{eff} and θ_{FL}^{eff} are (0.07 ± 0.01) and (0.02 ± 0.002) , respectively in agreement
190 with the previous reports^{6,33,40}. After post annealing at 400 °C, the reference Pt10 sample does
191 not show a SHH signal, suggesting that its SOT did not withstand such annealing.

192 As presented in Fig. 2e, θ_z^{eff} and θ_x^{eff} do not depend on the MnPd₃ film thickness as
193 θ_y^{eff} does. θ_{FL}^{eff} shown in Fig. 2d also does not show any specific MnPd₃ film thickness
194 dependence. The $\sigma_{zx}^{z,eff}$ value in MP12 sample is as large as $\sim 0.14 \times 10^5 \hbar/2e \Omega^{-1}\text{m}^{-1}$. $\sigma_{zx}^{z,eff}$ in
195 MP samples is comparable or better than recent reports on WTe₂/Py¹⁸ and Mn₃GaN/Py¹⁷. $\sigma_{zx}^{x,eff}$
196 in MP12 sample is $0.77 \times 10^5 \hbar/2e \Omega^{-1}\text{m}^{-1}$. These values of θ_k and σ_{ij}^k are largest among the
197 reported values as listed in Table 1. The difference in the thickness dependence of the $\theta_{x,y,z}^{eff}$
198 indicate that their origins are also different.

199 We also performed ST-FMR measurement on MP10 sample as a confirmation of the
200 observed SOT with SHH technique. The details of ST-FMR are presented in Supplementary 8

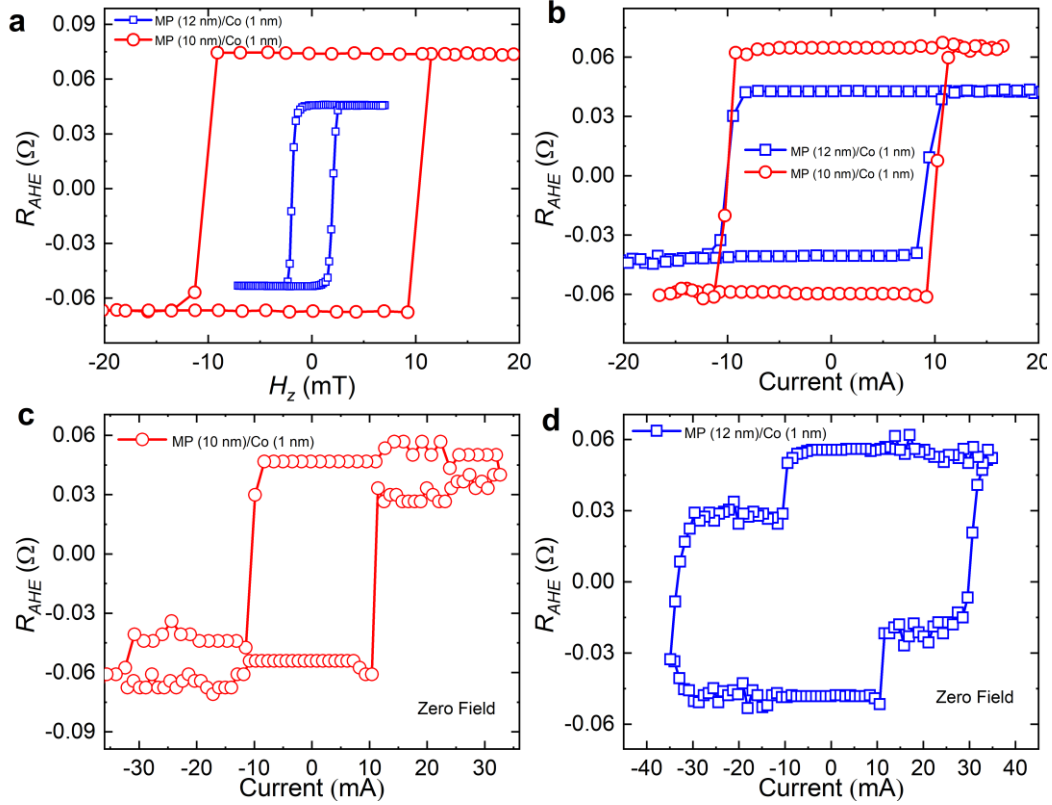
201 and Fig. S8. θ_y^{eff} estimated by using ST-FMR of MP10 sample is (0.21 ± 0.01) whereas it is
202 (0.22 ± 0.03) estimated using SHH. We also prepared reference samples Si/SiO₂/Pt (6 and 10
203 nm)/CoFeB (5 nm)/MgO (2 nm)/Ta (2 nm) (labelled as Pt6 and Pt10 samples) and Si/SiO₂/W (6
204 nm)/CoFeB (2 nm)/MgO (2 nm)/Ta (2 nm) (labelled as W sample) for the ST-FMR
205 measurements. θ_y^{eff} of as deposited Pt samples is 0.06 ± 0.01 and 0.08 ± 0.01 , respectively
206 (Supplementary 9 and Fig. S9). However, after post annealing at 400 °C the reference Pt samples
207 do not show a ST-FMR signal, suggesting that SOT did not withstand the annealing process.
208 θ_y^{eff} of as deposited W sample is determined to be -0.43 ± 0.03 at 6 GHz excitation frequency.
209 The estimated $\sigma_{zx}^{y,eff}$ is $-1.43 \times 10^5 \hbar/2e \Omega^{-1}m^{-1}$. This value of θ_y^{eff} of the as deposited W
210 sample is comparable to the previous report⁴¹. θ_y^{eff} of the W sample post annealed at 400 °C for
211 30 minutes is estimated to be -0.011 and the corresponding σ_y^{eff} is $-0.13 \times 10^5 \hbar/2e \Omega^{-1}m^{-1}$
212 (Supplementary 9 and Fig. S9).

213

Materials	ρ ($\mu\Omega\text{cm}$)	θ_x^{eff}	θ_y	θ_z^{eff}	θ_{FL}^{eff}	σ_{zx}^y ($\hbar/2e$ $10^5 \Omega^{-1}\text{m}^{-1}$)	J_{sw} (MA/cm^2)	Switched magnetic anisotropy	H_x (mT)	Post annealing temp ($^\circ\text{C}$)
This work	60 - 95	0.053	0.34-0.44	0.018	0.06	5.7-7.3	11-24.7	IMA-PMA	Zero	400
Pt ⁴⁰	40	-	0.14	-	0.08	3.5	50	PMA	70	As dep.
W ³⁸	188	-	-0.22	-	-0.022	-1.2	11 ⁴²	PMA	20	200 ⁴² -300 ³⁸
MnGaN ¹⁷	225	-0.013	0.025	0.018	-0.15	0.11	-	-	-	As dep.
WTe ₂ ¹⁸	380	-	0.03	0.013	0.034	0.08	-	-	-	As dep.

215

216 **Table 1: Summary of θ_k , σ_{ij}^k , and ρ of different spin channels post annealed at different**
217 **temperatures and measured at room temperature.**



218

219 **Fig. 3. Demonstration of external magnetic field-free out-of-plane magnetization switching**
 220 **via z -spin polarization generated anti-damping spin-orbit torque:** **a**, The anomalous Hall
 221 resistance as a function of out-of-plane external field. **b**, Switching of perpendicular Co layer via
 222 SOT under the application of -8 mT and -20 mT along x -direction for MP (10 nm)/Co (1 nm) and
 223 MP (12 nm)/Co (1 nm) samples, respectively. **c**, and **d**, Field-free perpendicular Co layer
 224 switching via out-of-plane anti-damping-like torque generated by z -spin polarization. The Hall
 225 bar with a length of 130 μm and a width of 10 μm was used for the magnetization switching
 226 experiment.

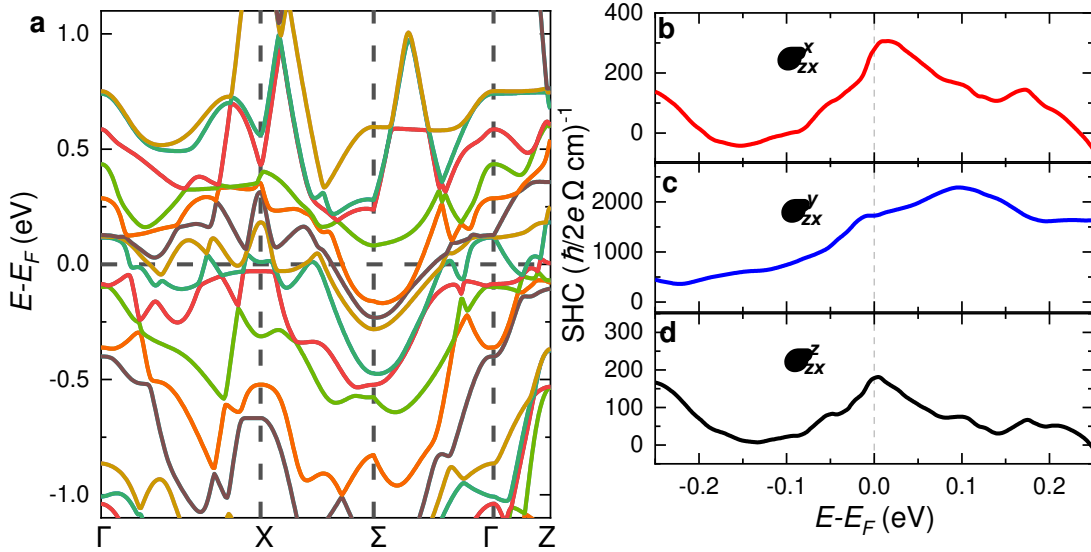
227 In order to demonstrate external magnetic field-free PMA switching, we prepared
 228 Si/SiO₂/MnPd₃ (10 and 12 nm)/Co (1 nm)/MgO (2 nm)/Ta (2 nm) samples (will be labelled as
 229 MP10/Co1 and MP12/Co1 samples). MP10/Co1 and MP12/Co1 samples were annealed at 400

230 °C for 30 minutes in vacuum and subsequently field-cooled under the application of an out-of-
231 plane magnetic field of 0.45 T. Fig. 3a shows anomalous Hall resistance (R_{AHE}) as a function of
232 out-of-plane magnetic field. The hysteretic R_{AHE} loop confirms PMA is present in the Co layer.
233 Alternatively, magnetometry was also used to confirm that PMA is present in MP10/Co1 sample
234 (Supplementary 3 and Fig. S3b). Fig. 3b shows current-induced SOT magnetization switching
235 under the presence of negative external magnetic fields. The write d.c. current pulse width used
236 for PMA switching is 20 ms, which is followed by a read current of 0.4 mA. The full switching
237 of magnetization occurs in MP10/Co1 and MP12/Co1 samples at ~ 10.1 mA and 9.5 mA,
238 respectively. Then, in the absence of external magnetic field, the d.c. current in pulses is swept
239 from -36 mA to + 36 mA with a step size of 1.06 mA. For MP10/Co1 as shown in Fig. 3c, partial
240 switching of the magnetization occurs at a positive current of about 10.78 mA, and complete
241 switching occurs at ~ 32.4 mA (~ 37.0 MA/cm²). In the subsequent reverse sweep partial
242 switching of magnetization occurs at ~ -10.87 mA and complete switching occurs at ~ -31.63
243 mA. For MP12/Co1 sample as shown in Fig. 3d, partial switching of magnetization occurs at a
244 positive current of ~ 11.35 mA. Continuously sweeping the d.c. pulses switches the remaining
245 magnetization at ~ 30.92 mA (~ 24.7 MA/cm²). Subsequently reverse sweeping the current
246 pulses, partial switching of magnetization occurs at ~ -9.60 mA and switching of remaining
247 magnetization occurs at ~ -33.32 mA. Since the R_{AHE} values obtained by field sweep and current
248 sweep are close, we can conclude that the full switching of PMA has been observed in both PMA
249 samples. J_{sw} values observed in our PMA samples without external magnetic field is comparable
250 or better than the previously reported values in Pt/Co^{5,6} (~ 23 -100 MA/cm²), Pd_{0.25}Pt_{0.75}/Co⁴³
251 (~ 22 MA/cm²), Pt/antiferromagnet⁴⁴ with external magnetic field. The SOT switching of
252 magnetization in our PMA samples results from the interplay of $\tau_{ADL,x}$, $\tau_{ADL,y}$, $\tau_{ADL,z}$, and τ_{FL} .

253 In the presence of external magnetic field the R_{AHE} vs I loop shows similar behavior as that of
 254 positive θ_y^{eff} such as in the case of Pt/Co/AlOx^{5,6}. In the absence of an external magnetic field, if
 255 there is only $\tau_{ADL,z}$, PMA switching occurs via anti-damping process, which is confirmed by
 256 numerically solving Landau-Lifshitz-Gilbert (LLG) equation (Supplementay 10 and Fig. S10b).
 257 In the presence of a relatively weaker $\tau_{ADL,z}$ and $\tau_{ADL,x}$ and strong $\tau_{ADL,y}$ the magnetization is
 258 partially switched at a lower current (~ 10 mA), which results in an intermediate state. The
 259 intermediate state can occur due to an insufficient external magnetic field, which is unable to
 260 completely break mirror symmetry⁴⁵. Previously, intermediate magnetic states were observed
 261 below threshold J_{sw} (Ref. ⁴⁶). The external magnetic field-free switching of PMA
 262 unambiguously demonstrates the presence of $\hat{\sigma}_z$ generated $\tau_{ADL,z}$ in the MP samples. These
 263 experimental results of PMA switching have been qualitatively reproduced by the LLG
 264 simulations (Supplementary 10 and Figs. S10c and S10d). The intermediate states observed
 265 could be utilized for neuromorphic computing¹³. In addition to field-free PMA switching, we
 266 also performed field-free magnetization switching of the in-plane CoFeB layer in MP24 sample,
 267 as detected by using unidirectional spin Hall magnetoresistance (USMR) mechanism^{47,48}
 268 (Supplementary 11 and Fig. S11). J_{sw} is estimated to be ~ 11.0 MA/cm² using the parallel resistor
 269 model.

270 We also performed SHH measurements on the PMA samples, as detailed in
 271 Supplementary 13 and Fig. s13. The magnitude of the SHH resistance ($R_{xy}^{2\omega}$) is not symmetric at
 272 up and down magnetizations when the field is swept along y-axis. If there were only τ_{FL} and τ_{Oe}
 273 present in MP samples, the magnitude and field dependence of $R_{xy}^{2\omega}$ would remain the same since
 274 the spin-orbit field associated to them is independent of the magnetization polarity as in the case
 275 of Ta/CoFeB/MgO²³. The spin-orbit field associated with $\tau_{ADL,x}$ ($\mathbf{H}_{ADL,x} \sim (\hat{\sigma}_x \times \hat{m})$) switches

276 sign as the magnetization switches sign, which results in the unequal and different field
 277 dependence of $R_{xy}^{2\omega}$. This clearly shows the presence of torque generated by $\hat{\sigma}_x$ in MP samples.
 278 θ_x^{eff} , θ_y^{eff} , and θ_{FL}^{eff} of the MP10/Co1 sample (MP12/Co1 sample) are 0.023 ± 0.001 ($0.040 \pm$
 279 0.003), 0.24 ± 0.02 (0.32 ± 0.03), and 0.03 ± 0.001 (0.12 ± 0.01), respectively. These values are
 280 comparable to the SHH-measured SOT efficiencies of IMA MP10 and MP12 samples.



281

282 **Fig. 4: Effect of (114) texture on the spin polarization.** **a**, The calculated band structure of
 283 stoichiometric MnPd₃ at room temperature. **b**, **c**, and **d**, The calculated σ_{zx}^x , σ_{zx}^y , and σ_{zx}^z as a
 284 function of energy for MnPd₃ (114) film, where the x axis is oriented along the $[\bar{4}01]$ direction.

285 We explain the appearance of the non-vanishing $\hat{\sigma}_x$ and $\hat{\sigma}_z$ in terms the contribution from
 286 grains of different orientations in our polycrystalline MnPd₃ films. MnPd₃ has crystal space
 287 group I4/mmm [32]. If the film was monocrystalline and (001) oriented with the charge current
 288 flowing along the [100] direction (the x -direction), only the conventional spin Hall conductivity
 289 σ_{zx}^y (where the spin current flows along the [001] direction (the z -direction) normal to the charge
 290 current and has spin polarization along the [010] direction (the y -direction)), would be allowed

291 due to the (001) plane being invariant to all symmetry operations of this space group. In a
 292 polycrystalline film, however, other crystal orientations with lower symmetries contribute to the
 293 spin Hall conductivity. For example, the (114) plane corresponding to the dominant texture of
 294 our films (reflected by the strongest XRD peak in Fig. 1 (b)) is only invariant with respect to
 295 mirror symmetry $M_{[\bar{1}10]}$ and two-fold rotation $C_{[\bar{1}10]}$. This allows the appearance of
 296 unconventional components of the spin Hall conductivity tensor, such as σ_{zx}^x and σ_{zx}^z , where the
 297 spin polarization is parallel to the direction of the spin current or the charge current. Moreover, in
 298 a polycrystalline film, the current direction itself varies with respect to the high symmetry
 299 directions of different grains, which also influences the shape of the spin Hall conductivity
 300 tensor. These aspects have been discussed in Ref. [15].

301 To quantitatively evaluate the contribution from this mechanism, we perform first-principles
 302 density functional theory calculations of spin Hall conductivity of bulk MnPd₃ assuming a room-
 303 temperature paramagnetic phase. Figure 4a shows the calculated band structure of MnPd₃. There
 304 are several bands crossing the Fermi level (E_F), indicating the metallic ground state. The small
 305 gaps between the bands near E_F are favorable for the sizable spin Hall conductivity⁴⁹, which is
 306 given by⁵⁰

$$307 \quad \sigma_{ij}^k = \frac{e^2}{\hbar} \int \frac{d^3\vec{k}}{(2\pi)^3} \sum_n f_{n\vec{k}} \Omega_{n,ij}^k(\vec{k}), \quad (3)$$

$$308 \quad \Omega_{n,ij}^k(\vec{k}) = -2Im \sum_{n' \neq n} \frac{\langle n\vec{k} | J_i^k | n'\vec{k} \rangle \langle n'\vec{k} | v_j | n\vec{k} \rangle}{(E_{n\vec{k}} - E_{n'\vec{k}})^2}, \quad (4),$$

309 where $f_{n\vec{k}}$ is the Fermi-Dirac distribution function for band n and wave vector \vec{k} , $\Omega_{n,ij}^k(\vec{k})$ is the
 310 spin Berry curvature, $J_i^k = \frac{1}{2}\{v_i, s_k\}$ is the spin current operator, v_i and s_k are velocity and spin
 311 operators, respectively, and $i, j, k = x, y, z$. As expected, for MnPd₃ textured in the (001) plane,

312 only the conventional σ_{zx}^y is non-vanishing (Table 2 in Supplementary 13). However, for the
 313 dominant (114) stacking texture, the unconventional spin Hall conductivities (σ_{zx}^x and σ_{zx}^z)
 314 emerge (Table 2 in Supplementary 13). Figures 4b-d show the calculated spin Hall
 315 conductivities for MnPd₃ (114) film as a function of energy when the charge current flows along
 316 the $[\bar{4}01]$ direction (the x -direction). We find a high conventional $\sigma_{zx}^y \sim 1744 \left(\frac{\hbar}{2e}\right) (\Omega \text{ cm})^{-1}$ and
 317 sizable unconventional conductivities $\sigma_{zx}^x \sim 279 \left(\frac{\hbar}{2e}\right) (\Omega \text{ cm})^{-1}$ and $\sigma_{zx}^z \sim 166 \left(\frac{\hbar}{2e}\right) (\Omega \text{ cm})^{-1}$ at
 318 the Fermi energy. It is evident that the σ_{zx}^x and σ_{zx}^z values are approximately an order of
 319 magnitude smaller than σ_{zx}^y , which is consistent with our experimental observation. Similarly,
 320 other MnPd₃ grains with different orientations can also contribute to the unconventional spin
 321 Hall conductivity.

322 In summary, we studied anti-damping spin-orbit torques generated by the $\hat{\sigma}_x$, $\hat{\sigma}_y$, and $\hat{\sigma}_z$
 323 in MnPd₃/ferromagnet heterostructure. At least two independent characterizations were
 324 performed to verify the presence of torques. DFT simulations confirmed the low crystal
 325 symmetry present in the (114) oriented MnPd₃ thin films as the origin of the observed
 326 unconventional SOTs. We demonstrated successful growth of conductive MnPd₃ thin films with
 327 high σ_{zx}^x , σ_{zx}^y , and σ_{zx}^z after post annealing at 400 °C for half an hour. Complete external
 328 magnetic field-free switching of both IMA and PMA were realized. The observed SOTs were
 329 robust against thermal treatment, and compatible with low damping constant of CoFeB even
 330 after post annealing. All of these are key factors for the integration of a practical spin current
 331 source based on MnPd₃ into next generation of SOT-based spintronics devices.

332

333 **References**

- 334 1. Dieny, B. *et al.* Opportunities and challenges for spintronics in the microelectronics
335 industry. *Nat. Electron.* **3**, 446–459 (2020).
- 336 2. Grimaldi, E. *et al.* Single-shot dynamics of spin–orbit torque and spin transfer torque
337 switching in three-terminal magnetic tunnel junctions. *Nat. Nanotechnol.* **15**, 111–117
338 (2020).
- 339 3. Manchon, A. *et al.* Current-induced spin-orbit torques in ferromagnetic and
340 antiferromagnetic systems. *Rev. Mod. Phys.* **91**, 035004 (2019).
- 341 4. Chernyshov, A. *et al.* Evidence for reversible control of magnetization in a ferromagnetic
342 material via spin-orbit magnetic field. *Nat. Phys.* **5**, 656 (2008).
- 343 5. Miron, I. M. *et al.* Perpendicular switching of a single ferromagnetic layer induced by in-
344 plane current injection. *Nature* **476**, 189–193 (2011).
- 345 6. Liu, L., Lee, O. J., Gudmundsen, T. J., Ralph, D. C. & Buhrman, R. A. Current-induced
346 switching of perpendicularly magnetized magnetic layers using spin torque from the spin
347 hall effect. *Phys. Rev. Lett.* **109**, 096602 (2012).
- 348 7. Fukami, S., Anekawa, T., Zhang, C. & Ohno, H. A spin-orbit torque switching scheme
349 with collinear magnetic easy axis and current configuration. *Nat. Nanotechnol.* **11**, 621–
350 626 (2016).
- 351 8. Mellnik, A. R. *et al.* Spin-transfer torque generated by a topological insulator. *Nature* **511**,
352 449–451 (2014).
- 353 9. Fan, Y. *et al.* Magnetization switching through giant spin-orbit torque in a magnetically

- 354 doped topological insulator heterostructure. *Nat. Mater.* **13**, 699–704 (2014).
- 355 10. Kondou, K. *et al.* Fermi level dependent charge-to-spin current conversion by Dirac
356 surface state of topological insulators. *Nat. Phys.* **12**, 1027–1032 (2016).
- 357 11. DC, M. *et al.* Room-temperature high spin-orbit torque due to quantum confinement in
358 sputtered $\text{Bi}_x\text{Se}_{(1-x)}$ films. *Nat. Mater.* **17**, 800–807 (2018).
- 359 12. Khang, N., Khang, D., Ueda, Y. & Hai, P. N. A conductive topological insulator with
360 large spin Hall effect for ultralow power spin-orbit torque switching. *Nat. Mater.* **17**, 808–
361 813 (2018).
- 362 13. Fukami, S., Zhang, C., DuttaGupta, S., Kurenkov, A. & Ohno, H. Magnetization
363 switching by spin–orbit torque in an antiferromagnet–ferromagnet bilayer system. *Nat.*
364 *Mater.* **15**, 535–541 (2016).
- 365 14. Oh, Y. W. *et al.* Field-free switching of perpendicular magnetization through spin-orbit
366 torque in antiferromagnet/ferromagnet/oxide structures. *Nat. Nanotechnol.* **11**, 878–884
367 (2016).
- 368 15. Zhang, W. *et al.* Giant facet-dependent spin-orbit torque and spin Hall conductivity in the
369 triangular antiferromagnet IrMn_3 . *Sci. Adv.* **2**, (2016).
- 370 16. Chen, J.-Y. *et al.* Field-free spin-orbit torque switching of composite perpendicular
371 $\text{CoFeB}/\text{Gd}/\text{CoFeB}$ layers utilized for three-terminal magnetic tunnel junctions. *Appl. Phys.*
372 *Lett.* **111**, 012402 (2017).
- 373 17. Nan, T. *et al.* Controlling spin current polarization through non-collinear
374 antiferromagnetism. *Nat. Commun.* **11**, (2020).

- 375 18. Macneill, D. *et al.* Control of spin–orbit torques through crystal symmetry in WTe₂
376 /ferromagnet bilayers. *Nat. Phys.* **13**, 300–306 (2017).
- 377 19. Shi, S. *et al.* All-electric magnetization switching and Dzyaloshinskii–Moriya interaction
378 in WTe₂/ferromagnet heterostructures. *Nat. Nanotechnol.* **14**, 945–949 (2019).
- 379 20. Song, P. *et al.* Coexistence of large conventional and planar spin Hall effect with long spin
380 diffusion length in a low-symmetry semimetal at room temperature. *Nat. Mater.* **19**, 292–
381 298 (2020).
- 382 21. Qi, X.-L. & Zhang, S.-C. Topological insulators and superconductors. *Rev. Mod. Phys.* **83**,
383 1057–1106 (2011).
- 384 22. Zhao, B. *et al.* Unconventional charge–spin conversion in weyl-semimetal WTe₂. *Adv.*
385 *Mater.* **2000818** (2020).
- 386 23. Baek, S. C. *et al.* Spin currents and spin–orbit torques in ferromagnetic trilayers. *Nat.*
387 *Mater.* **17**, 509–513 (2018).
- 388 24. Lee, D. & Lee, K. Spin-orbit Torque Switching of Perpendicular Magnetization in
389 Ferromagnetic Trilayers. *Sci. Rep.* **10**, 1772 (2020).
- 390 25. Li, X. *et al.* Materials Requirements of High-Speed and Low-Power Spin-Orbit-Torque
391 Magnetic Random-Access Memory. *IEEE J. Electron Devices Soc.* **8**, 674 - 680 (2020).
- 392 26. Mangin, S. *et al.* Current-induced magnetization reversal in nanopillars with perpendicular
393 anisotropy. *Nat. Mater.* **5**, 210–215 (2006).
- 394 27. Han, J. *et al.* Room-temperature spin-orbit torque switching induced by a topological

- 395 insulator. *Phys. Rev. Lett.* **119**, 077702 (2017).
- 396 28. Li, P. *et al.* Magnetization switching using topological surface states. *Sci. Adv.* **5**, (2019).
- 397 29. Zhao, Z., Smith, A. K., Jamali, M. & Wang, J. P. External-field-free spin Hall switching
398 of perpendicular magnetic nanopillar with a dipole-coupled composite structure. *Adv.*
399 *Electron. Mater.* **6**, 1901368 (2020).
- 400 30. Krizakova, V., Garello, K., Grimaldi, E., Kar, G. S. & Gambardella, P. Field-free
401 switching of magnetic tunnel junctions driven by spin-orbit torques at sub-ns timescales.
402 *Appl. Phys. Lett.* **116**, 232406 (2020).
- 403 31. Wang, M. *et al.* Field-free switching of a perpendicular magnetic tunnel junction through
404 the interplay of spin-orbit and spin-transfer torques. *Nat. Electron.* **1**, 582–588 (2018).
- 405 32. Coldea, M. *et al.* X-ray photoelectron spectroscopy and magnetism of Mn-Pd alloys. *J.*
406 *Alloys Compd.* **417**, 7–12 (2006).
- 407 33. Avci, C. O. *et al.* Interplay of spin-orbit torque and thermoelectric effects in
408 ferromagnet/normal-metal bilayers. *Phys. Rev. B* **90**, 224427 (2014).
- 409 34. Chen, Y.-T. *et al.* Theory of spin Hall magnetoresistance. *Phys. Rev. B* **87**, 144411 (2013).
- 410 35. Zhang, W., Han, W., Jiang, X., Yang, S.-H. & Parkin, S. S. P. Role of transparency of
411 platinum-ferromagnet interfaces in determining the intrinsic magnitude of the spin Hall
412 effect. *Nat. Phys.* **11**, 496–503 (2015).
- 413 36. Pai, C. F., Ou, Y., Vilela-Leão, L. H., Ralph, D. C. & Buhrman, R. A. Dependence of the
414 efficiency of spin Hall torque on the transparency of Pt/ferromagnetic layer interfaces.

- 415 *Phys. Rev. B* **92**, 064426 (2015).
- 416 37. Zhang, W. *et al.* Spin Hall effects in metallic antiferromagnets. *Phys. Rev. Lett.* **113**,
417 196602 (2014).
- 418 38. Okada, A. *et al.* Spin-pumping-free determination of spin-orbit torque efficiency from
419 spin-torque ferromagnetic resonance. *Phys. Rev. Appl.* **12**, 014040 (2019).
- 420 39. Zhu, L., Ralph, D. C. & Buhrman, R. A. Spin-Orbit Torques in Heavy-Metal-Ferromagnet
421 Bilayers with Varying Strengths of Interfacial Spin-Orbit Coupling. *Phys. Rev. Lett.* **122**,
422 77201 (2019).
- 423 40. Feng, J. *et al.* Effects of oxidation of top and bottom interfaces on the electric, magnetic,
424 and spin-orbit torque properties of Pt / Co / Al Ox trilayers. *Phys. Rev. Appl.* **13**, 044029
425 (2020).
- 426 41. Pai, C. F. *et al.* Spin transfer torque devices utilizing the giant spin Hall effect of tungsten.
427 *Appl. Phys. Lett.* **101**, 122404 (2012).
- 428 42. Cho, S., Chris Baek, S., Lee, K.-D., Jo, Y. & Park, B.-G. Large spin Hall
429 magnetoresistance and its correlation to the spin-orbit torque in W/CoFeB/MgO
430 structures. *Sci. Rep.* **5**, 14668 (2015).
- 431 43. Zhu, L. *et al.* Strong damping-like spin-orbit torque and tunable Dzyaloshinskii–Moriya
432 interaction generated by Low-resistivity Pd_{1-x}Pt_x alloys. *Adv. Funct. Mater.* **29**, 1805822
433 (2019).
- 434 44. Tsai, H. *et al.* Electrical manipulation of a topological antiferromagnetic state. *Nature* **580**,
435 608 (2020).

- 436 45. Cao, J. *et al.* Spin-orbit torque induced magnetization switching in Ta/Co₂₀Fe₆₀B₂₀/MgO
437 structures under small in-plane magnetic fields. *Appl. Phys. Lett.* **108**, 172404 (2016).
- 438 46. Baumgartner, M. *et al.* Spatially and time-resolved magnetization dynamics driven by
439 spin-orbit torques. *Nat. Nanotechnol.* **12**, 980–986 (2017).
- 440 47. Avci, C. O. *et al.* Unidirectional spin Hall magnetoresistance in ferromagnet/normal metal
441 bilayers. *Nat. Phys.* **11**, 570–575 (2015).
- 442 48. Lv, Y. *et al.* Large unidirectional spin Hall and Rashba-Edelstein magnetoresistance in
443 topological insulator/magnetic insulator heterostructures. arXiv:1806.09066. (2018).
- 444 49. Guo, G. Y., Murakami, S., Chen, T.-W. & Nagaosa, N. Intrinsic spin Hall effect in
445 platinum: first-principles calculations. **100**, 096401 (2008).
- 446 50. Sinova, J., Valenzuela, S. O., Wunderlich, J., Back, C. H. & Jungwirth, T. Spin Hall
447 effects. *Rev. Mod. Phys.* **87**, 1213–1260 (2015).

448 **Acknowledgments**

449 This research was supported in part by ASCENT, one of six centers in JUMP, a Semiconductor
450 Research Corporation (SRC) program sponsored by DARPA. The authors thank the NSF Center
451 for Energy Efficient Electronics Science (E3S) and TSMC for financial support. Part of this
452 work was performed at the Stanford Nano Shared Facilities (SNSF)/Stanford Nanofabrication
453 Facility (SNF), supported by the National Science Foundation under award ECCS-1542152. The
454 research at the University of Nebraska-Lincoln is supported by the National Science Foundation
455 through the Nebraska Materials Science and Engineering Center (MRSEC, Grant No. DMR-
456 1420645). P. Q. acknowledges support from the National Research Council Research
457 Associateship Program. S.E. and M. B. V. acknowledge funding from NSF award DMR-

458 1905909, and assistance from Randy Dumas at Quantum Design with VSM measurements. The
459 authors would also like to acknowledge Dr. Carlos H. Diaz, Dr. Peng Li, and Dr. Juliet
460 Jamtgaard for fruitful discussions.

461 **Author contributions**

462 M. DC conceived, designed, and coordinated the research with contributions from M.M., S.-J.L.,
463 W.T., and S.X.W. S.X.W supervised the study. M. DC grew thin films, performed XRD
464 measurement, fabricated Hall bar, ST-FMR device, carried out ST-FMR, SHH, and switching
465 measurements with contributions from Y.D., X.L., C.B., F.X., and Y-L. H. D-F. S. and E. T.
466 performed DFT calculations. V.D.H., A. H., and W. W. carried out TEM and EDS studies. A.V.
467 performed pole figure measurements. M. B.V. and S.E. performed magnetometry measurements.
468 P.Q., B.K., and J.B. performed PNR measurements and modelling. M. DC performed LLG
469 simulations. M. DC performed data analysis and wrote the manuscript with contributions from
470 D-F. S, P.Q., A.V., and S.X.W. All authors discussed the results and commented on the
471 manuscript.

472 **Online content**

473 Any methods, additional references, Nature Research reporting summaries, source data,
474 Supplementary, supplementary information, acknowledgements, peer review information; details
475 of author contributions and competing interests; and statements of data and code availability are
476 available online.

477 **Competing Interests**

478 The authors declare no competing interests.

479 **Data Availability**

480 The data that support the findings of this study are available from the corresponding authors on
481 reasonable request.

482

483 **Methods**

484 **Sample growth and thin film characterization**

485 Manganese Palladium (MnPd_3) thin films for the magneto-transport, SOT
486 characterization, and magnetization switching were grown on Si/SiO₂ substrate at room
487 temperature by sputtering a composite MnPd_2 (99.99% pure) target in AJA sputtering system⁵¹
488 with a base pressure of 2.0×10^{-8} Torr. MnPd_3 , CoFeB, Pt, and Ta were dc sputtered at 25 W
489 power with deposition rates 0.27, 0.056, 0.27, and 0.07 Å/s, respectively. The MgO layer was rf
490 sputtered at 50 W power with a deposition rate of 0.013 Å/s.

491 The thin section for transmission electron microscopy (TEM) was prepared by the focus
492 ion beam with FEI Helios Nanolab 660⁵¹. The TEM analysis was carried out by a Hitachi HF-
493 5000 equipped with a probe aberration corrector, under 200 kV. Bright field (BF), secondary
494 electron (SE) and Annular (both medium and high angle) dark field (ADF) images were captured
495 simultaneously in scanning TEM (STEM) mode. High resolution energy dispersive X-ray
496 spectroscopy (EDS) mapping and line scan were performed by an Oxford Instruments large solid
497 angle (2.0 sr) dual windowless detectors⁵¹.

498 **Device fabrication and electrical characterization**

499 The multilayer thin films were patterned into Hall bars for the quantum transport, SHH,
500 and magnetization switching experiments using an optical lithography process. The width and
501 length of Hall bar was 10 μm and length 130 μm, respectively. The separation between the Hall-
502 crosses in Hall bar device is 37 μm. For the ST-FMR measurement thin films were patterned into
503 rectangular strips of dimension 25-30 μm length and width, respectively. After the first step of
504 photolithography, the Ar ion mill was used to define the device geometry. Ti (10 nm)/Au (150

505 nm) thick electrical contacts were deposited after the second step of lithography using KJL e-
506 beam evaporator. A physical property measurement system (PPMS)⁵¹ was used to measure the
507 electrical properties. Two Lockins SR830⁵¹ and 6221 current source⁵¹ were used to probe first
508 and second harmonic voltage and supply current, respectively. An Agilent HP 83620B⁵¹ was
509 used to supply the r.f. current for the ST-FMR measurements. The d.c. voltage was measured
510 with a Keithley 2000 multi-meter⁵¹.

Figures

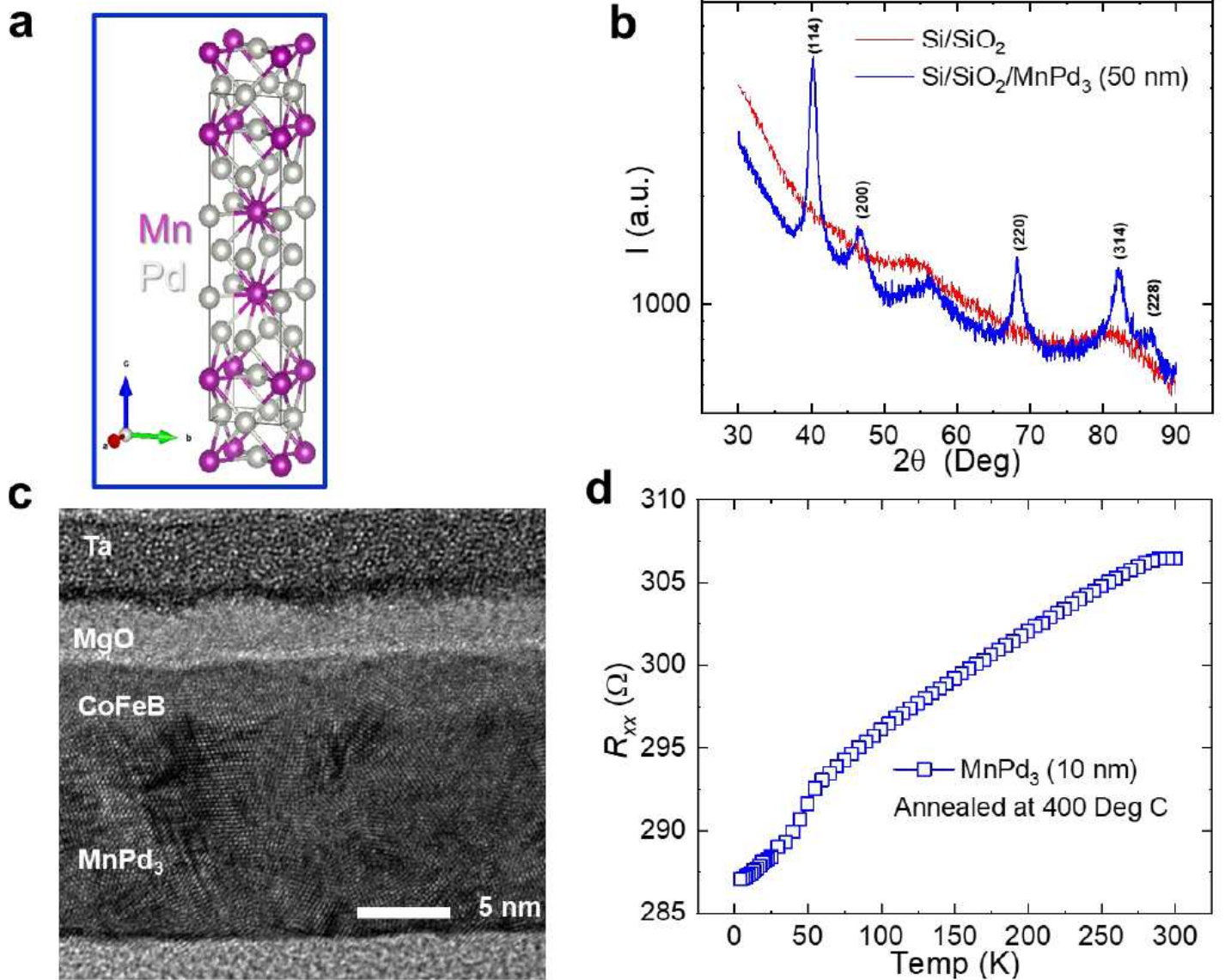


Figure 1

Characterization of MnPd₃ thin film: a, Schematic diagram of D023 MnPd₃ unit cell. b, XRD of Si/SiO₂/MnPd₃ (50 nm) film, post-annealed at 400 °C for 30 min. c, Cross-section TEM image of Si/SiO₂/MnPd₃ (10 nm)/CoFeB (5 nm)/MgO (2 nm)/Ta (2 nm) sample. d, Four terminal resistance as a function of temperature of Si/SiO₂/MnPd₃ (10 nm) sample.

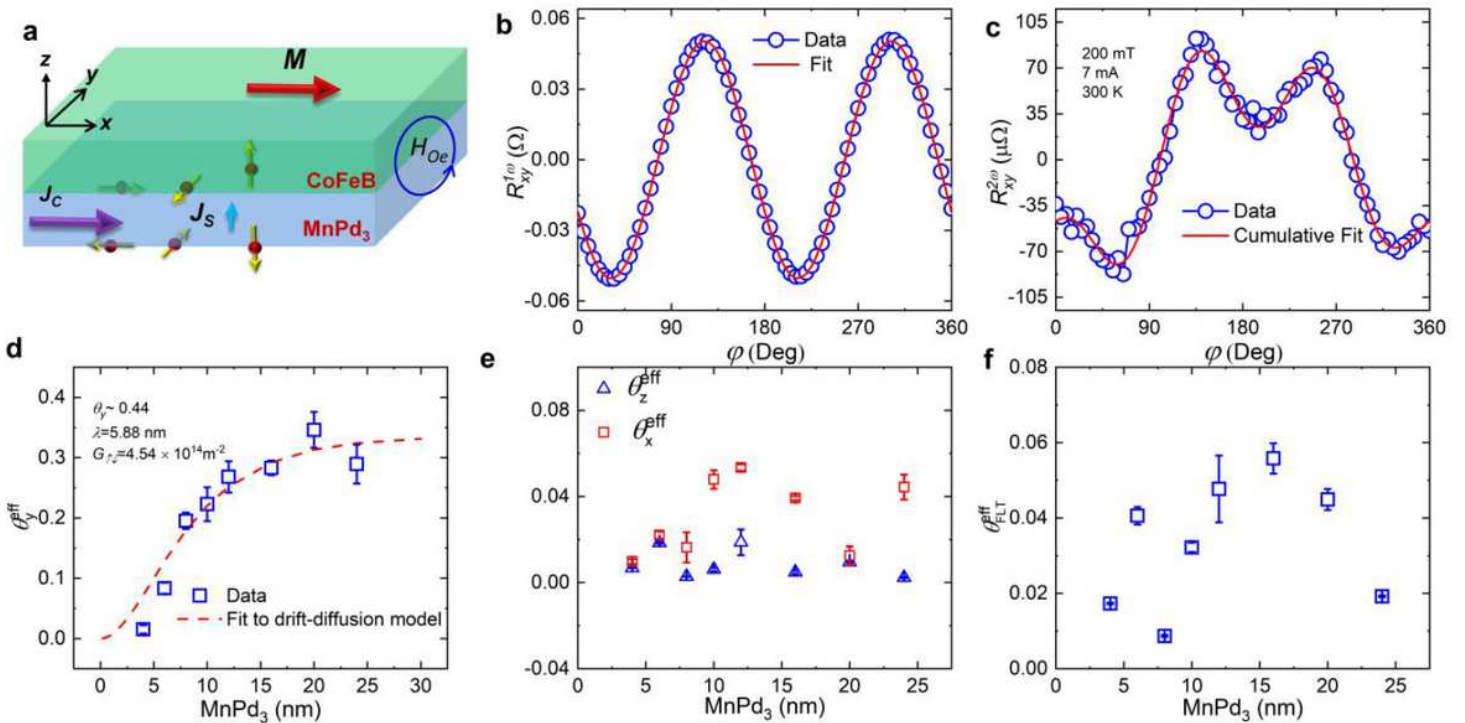


Figure 2

SOT characterization using Second Harmonic Hall (SHH) technique on Si/SiO₂/MnPd₃ (x nm)/CoFeB (5 nm)/MgO (2 nm)/Ta (2 nm): a, Schematic diagram showing in-plane charge current generated spin current with spin polarizations along three axes. The red spheres represent electrons and yellow arrows represent spin magnetic moment, respectively. b, and c, R_{xy}^{1st} and R_{xy}^{2nd} , respectively, as a function of in-plane magnetic field rotation at a fixed amplitude of 200 mT in MP12 sample. d, e, and f, Effective spin torque efficiency due to the in-plane anti-damping-like, in-plane and out-of-plane anti-damping-like and field-like torques, respectively, as a function of MnPd₃ film thickness. The Hall bar device used for this measurement was 10 μm wide and 130 μm long, respectively.

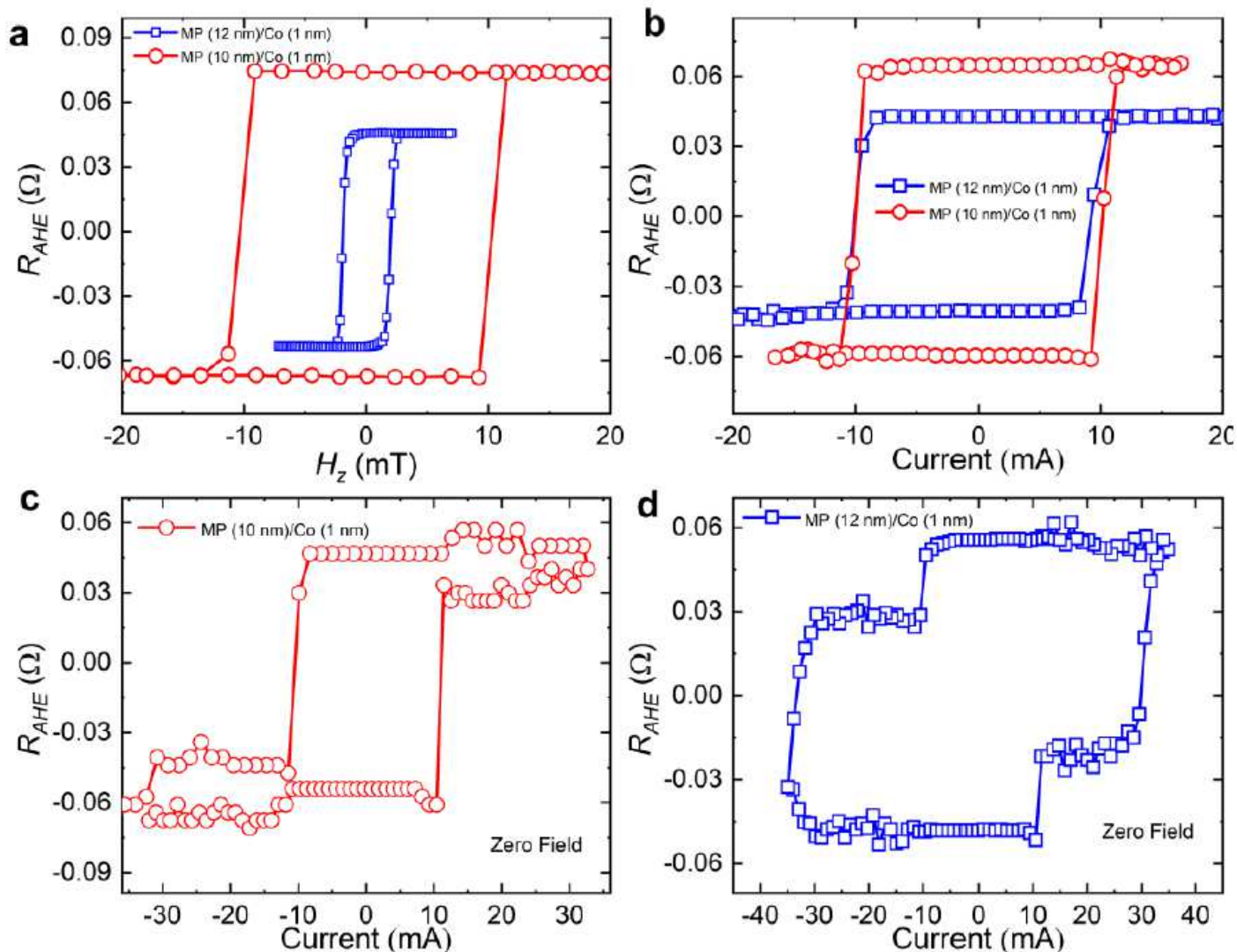


Figure 3

Demonstration of external magnetic field-free out-of-plane magnetization switching via z-spin polarization generated anti-damping spin-orbit torque: a, The anomalous Hall resistance as a function of out-of-plane external field. b, Switching of perpendicular Co layer via SOT under the application of -8 mT and -20 mT along x-direction for MP (10 nm)/Co (1 nm) and MP (12 nm)/Co (1 nm) samples, respectively. c, and d, Field-free perpendicular Co layer switching via out-of-plane anti-damping-like torque generated by z-spin polarization. The Hall bar with a length of 130 μm and a width of 10 μm was used for the magnetization switching experiment.

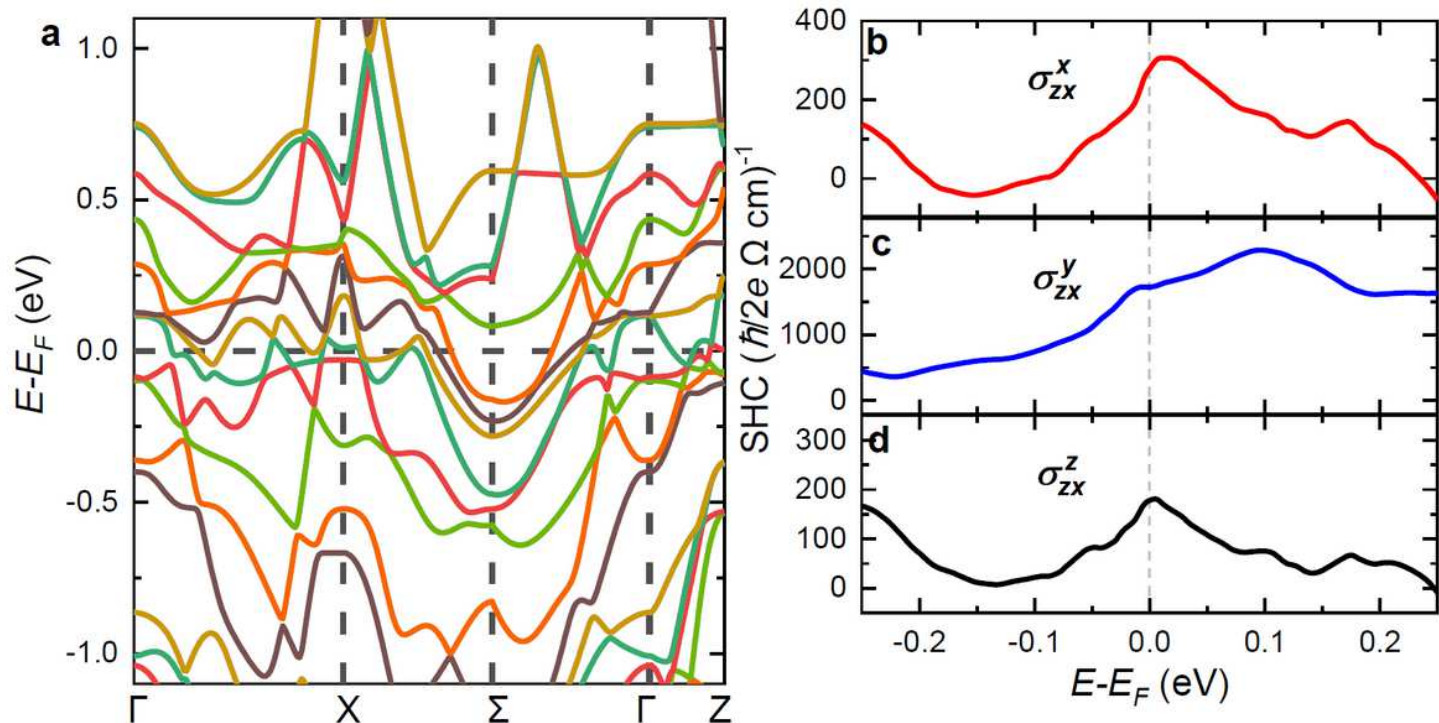


Figure 4

Effect of (114) texture on the spin polarization. a, The calculated band structure of stoichiometric MnPd3 at room temperature. b, c, and d, The calculated σ_{zx}^x , σ_{zx}^y , and σ_{zx}^z as a function of energy for MnPd3 (114) film, where the x axis is oriented along the [01] direction.

Supplementary Files

This is a list of supplementary files associated with this preprint. Click to download.

- [SupplementaryInformationV7.pdf](#)